

Contrasted Sn Substitution effects on Dirac line node semimetals SrIrO_3 and CaIrO_3

Masamichi Negishi,¹ Naoka Hiraoka,¹ Daisuke Nishio-Hamane,² and Hidenori Takagi^{1,3,4, a)}

¹⁾*Department of Physics, University of Tokyo, 7-3-1 Hongo, Bunkyo-ku, Tokyo 113-0033,*

Japan

²⁾*Institute for Solid State Physics, University of Tokyo, 5-1-5 Kashiwanoha, Kashiwa, Chiba 277-8581,*

Japan

³⁾*Max Planck Institute for Solid State Research, Heisenbergstraße 1, 70569 Stuttgart,*

Germany

⁴⁾*Institute for Functional Matter and Quantum Technologies, University of Stuttgart, Pfaffenwaldring 57, 70550 Stuttgart, Germany*

(Dated: 14 November 2019)

Perovskite-type iridates SrIrO_3 and CaIrO_3 are a Dirac line node semimetal protected by crystalline symmetry, providing an interesting playground to investigate electron correlation effects on topological semimetals. The effect of Sn doping was examined by growing $\text{SrIr}_{1-x}\text{Sn}_x\text{O}_3$ and $\text{CaIr}_{1-x}\text{Sn}_x\text{O}_3$ thin films epitaxially on $\text{SrTiO}_3(001)$ substrate using pulsed laser deposition. Upon Sn doping, the semimetallic ground state switches into an insulator. As temperature is lowered, the resistivity, $\rho(T)$, of $\text{SrIr}_{1-x}\text{Sn}_x\text{O}_3$ above a critical doping level ($x_c \sim 0.1$) shows a well-defined transition from the semimetal to a weakly ferromagnetic insulator at $T = T_c$. In contrast, the $\rho(T)$ of $\text{CaIr}_{1-x}\text{Sn}_x\text{O}_3$ with increasing x shows a rapid increase of magnitude but does not show clear signature of metal-insulator transition in the temperature dependence. We argue that the contrasted behavior of the two closely related iridates reflects the interplay between the effects of electron correlation and disorder enhanced by Sn doping.

Recently $5d$ iridium oxides with perovskite-related structures have been explored extensively as a mine for exotic quantum phases, partly because of an interplay of strong spin-orbit interaction and electron correlation of the $5d$ electrons¹. The strong spin-orbit coupling of ~ 0.4 eV for $5d$ electrons, which is larger than the typical crystal field splitting of $\lesssim 0.1$ eV within t_{2g} ², splits the t_{2g} bands with five d electrons into upper half-filled $J_{\text{eff}} = 1/2$ band and lower completely filled $J_{\text{eff}} = 3/2$ bands. In the two-dimensional layered perovskite Sr_2IrO_4 , a modest on-site Coulomb U of ~ 2 eV³ brings the system to a spin-orbital Mott state with the $J_{\text{eff}} = 1/2$ moments^{4,5}. Such a spin-orbital Mott state has been identified in many two-dimensional layered iridium oxides, where exotic magnetism of $J_{\text{eff}} = 1/2$, particularly the Kitaev spin liquid state, has been explored⁶. In the three-dimensional perovskites SrIrO_3 and CaIrO_3 , in contrast, the $J_{\text{eff}} = 1/2$ band remains metallic marginally due to the increased band width³ and forms a “correlated” topological semimetal.

SrIrO_3 and CaIrO_3 have a GdFeO_3 -type distorted perovskite structure where the rotation and the buckling of IrO_6 octahedra give rise to a unit cell with the size of $\sqrt{2}a_c \times \sqrt{2}a_c \times 2a_c$ (a_c is the lattice constant of the original cubic lattice) as shown in Fig. 1a^{7,8}. The results of band calculations indicate that SrIrO_3 and CaIrO_3 have Dirac electron bands with a line of nodes and heavy hole bands at the Fermi level⁹. The line nodes of Dirac bands are protected by the time-reversal symmetry and the gliding symmetry of the GdFeO_3 -type perovskite structure¹⁰. The existence of Dirac electrons has been supported by experiments, for example, by ARPES^{11,12} and transport measurements^{13,14}. Their proximity to the spin-orbital Mott state and moderately strong

electron correlations are evident, for example, from the observation of a transition from a Dirac semimetal to a magnetic insulator by decreasing the number of SrIrO_3 layers in $(\text{SrIrO}_3)_n, (\text{SrTiO}_3)_1$ superlattice structures¹⁵. The presence of an apparent correlation effect is a prominent feature of the two Ir perovskites when compared with many other topological semimetals which are only weakly correlated, and makes them an interesting arena to explore the effect of electron correlation in topological semimetals. As the ionic radius of Ca^{2+} (1.34 Å) is smaller than that of Sr^{2+} (1.44 Å)¹⁶, the lattice is more distorted in CaIrO_3 than in SrIrO_3 , which reduces the band width of CaIrO_3 appreciably as compared with that of SrIrO_3 . The effect of electron correlation should be larger in CaIrO_3 than SrIrO_3 . Recently, it was shown that the strong electron correlation modifies the semimetallic band structures appreciably in the two three-dimensional iridium perovskites. The stronger electron correlation effects of CaIrO_3 bring its Fermi level closer to the Dirac node and therefore further reduces its density of electrons and holes when compared to SrIrO_3 ¹⁴.

A transition from the Dirac semimetal to a magnetic insulator was also discovered in bulk polycrystalline SrIrO_3 by substituting Ir with Sn¹⁷. As Sn ions are tetravalent like Ir ions in SrIrO_3 , Sn doping does not change the valence of Ir ions and therefore reduces the hopping path of the Ir $5d$ electrons in real space, and hence the effective width of $J_{\text{eff}} = 1/2$ band, as in the case of the superlattice structure. We note here that Sn doping should modify not only the effective band width, but also the degree of disorder. With this unique opportunity of controlling the electron correlations and disorder in mind, we synthesized epitaxial thin films of $\text{SrIr}_{1-x}\text{Sn}_x\text{O}_3$ and $\text{CaIr}_{1-x}\text{Sn}_x\text{O}_3$ and measured their resistivity to probe the effects of Sn doping. A transition from a semimetal to a (magnetic) insulator is observed in both $\text{SrIr}_{1-x}\text{Sn}_x\text{O}_3$ and

^{a)}E-mail: h.takagi@fkf.mpg.de

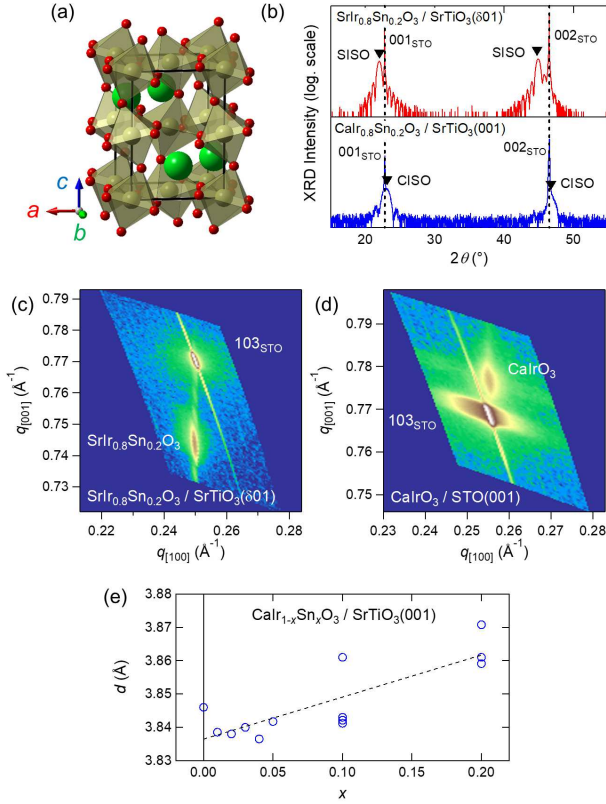


Fig. 1. (a) Crystal structure of perovskite-type SrIrO₃. The green, yellow, and red balls indicate Sr, Ir, O atoms, respectively. The black box indicates the GdFeO₃-type unit cell. (b) XRD 2θ - θ scans of SrIr_{0.8}Sn_{0.2}O₃ and CaIr_{0.8}Sn_{0.2}O₃ thin films. (c, d) XRD-RSM around 103_{STO} Bragg peak of SrIr_{0.8}Sn_{0.2}O₃ and CaIrO₃, indicating the in-plane lattice constant is locked to the substrate. The lattice constant for SrIr_{0.8}Sn_{0.2}O₃ along the other in-plane direction [010]_{STO} is confirmed to be also fixed to the substrate. (e) The out-of-plane lattice constant d of CaIr_{1-x}Sn_xO₃ films. The black dashed line, the result of linear fitting, shows $\sim 0.7\%$ increase from $x = 0$ to 0.2.

CaIr_{1-x}Sn_xO₃ thin films, as in the bulk SrIr_{1-x}Sn_xO₃. We discovered a sharp contrast in the transition behavior between the Sr and Ca iridium perovskites: the appearance of well-defined transition from the Dirac semimetal to a magnetic insulator as function of temperature above a critical Sn concentration $x_c \sim 0.1$ for SrIrO₃, and the continuous increase of resistivity without a clear signature of the semimetal-insulator transition for CaIrO₃, which we ascribe to the interplay of the electron correlation and the disorder effect.

SrIr_{1-x}Sn_xO₃ and CaIr_{1-x}Sn_xO₃ thin films were epitaxially grown in the range of $0 \leq x \leq 0.2$ on SrTiO₃(001) substrates by pulsed laser deposition technique using polycrystalline targets with 5 % excess B (Ir/Sn) cations. The film deposition of SrIr_{1-x}Sn_xO₃ (CaIr_{1-x}Sn_xO₃) was conducted at 650 °C (750 °C) in a 100 mTorr O₂ atmosphere. Typical thickness of our samples estimated from X-ray reflectivity measurement is ~ 15 nm (10 nm). Magnetization and transport measurements were conducted using a commercial SQUID magne-

Table I. The bulk lattice parameters of SrIrO₃ and CaIrO₃ and their matching to the cubic lattice parameter of SrTiO₃ ($a_{\text{STO}} = 3.905$ Å).

	a	b	c	$\frac{a_{\text{pc}}}{a_{\text{STO}}} - 1$	$\frac{c_{\text{pc}}}{a_{\text{STO}}} - 1$
SrIrO ₃ ¹⁸	5.597(1) Å	5.581(1) Å	7.752(2) Å	+1.2 %	-0.7 %
CaIrO ₃ ¹⁴	5.3597(5) Å	5.6131(4) Å	7.6824(8) Å	-0.6 %	-1.6 %

tometer (MPMS, Quantum Design) and in a physical property measurement system (PPMS, Quantum Design). The X-ray diffraction (XRD) measurements were performed using SmartLab, Rigaku.

The results of 2θ - θ scans of XRD indicate that all the grown SrIr_{1-x}Sn_xO₃ and CaIr_{1-x}Sn_xO₃ films crystallize in the perovskite structure without any trace of impurity phase within the given resolution (Fig. 1b). The full width at half maximum of the rocking curve is typically as narrow as 0.1° at the pseudo-cubic (001) peak and the Laue oscillations around the Bragg peaks are clearly observed. Reciprocal space mapping (RSM) measurements reveal that the in-plane lattice of the films is locked to that of the SrTiO₃ substrate (Figs. 1c, d). Those observations clearly demonstrate the epitaxial growth and high crystallinity of the grown films. The out-of-plane lattice constant of the CaIr_{1-x}Sn_xO₃ films as a function of Sn content x , as an average, increases almost 0.7 % from $x = 0$ to $x = 0.2$ which should reflect the larger ionic radius of Sn⁴⁺ (0.690 Å) than that of Ir⁴⁺ (0.625 Å)¹⁶ (Fig. 1e)

The film orientation was identified by RSM measurements of XRD and transition electron microscopy (Figs. 2a-c). We will describe the lattice orientation of films by the pseudo-cubic unit cell in this paper using lattice parameters $a_{\text{pc}} = \sqrt{a^2 + b^2}/2$ and $c_{\text{pc}} = c/2$, where a , b and c denote the orthorhombic unit cell parameters of the distorted GdFeO₃ structure¹⁹. In case of SrIr_{1-x}Sn_xO₃, the c_{pc} axis (|| orthorhombic c) lies within the substrate plane independent of Sn doping (Fig. 2d). This is natural because c_{pc} is closer to that of SrTiO₃ substrate than a_{pc} (See Table I.). In contrast, a_{pc} is closer to that of SrTiO₃ in CaIrO₃. The c_{pc} axis (|| orthorhombic c) therefore aligns perpendicular to the substrate plane in the CaIrO₃ case (Fig. 2f)²⁰. The inclusion of minority domains with the c_{pc} axis lying within the substrate plane as in SrIr_{1-x}Sn_xO₃ are observed for the high Sn content films ($x \geq 0.1$) (Fig. 2g), which very likely reflects the expansion of c_{pc} due to Sn doping and the resultant proximity to the lattice constant of SrTiO₃.

As a_{pc} is larger than c_{pc} , the orientation of c_{pc} within the substrate plane can be controlled by introducing additional epitaxial strain using step edges of vicinal substrate^{21,22}. We used a vicinal SrTiO₃(δ01) substrate with the substrate plane 0.4° rotated from (001) towards the [100] direction for the growth of SrIr_{1-x}Sn_xO₃. Because of the epitaxial strain from the side (100) plane at the step edges, the c_{pc} (|| orthorhombic c) axis prefers to align along the edge, namely [010]_{STO} direction (Fig. 2e). The RSM measurements clearly indicate that more than 95 % of domains have c_{pc} axis parallel to the substrate [010] direction for the films on the vicinal substrates. Consistent with the in-plane preferred orientation, a

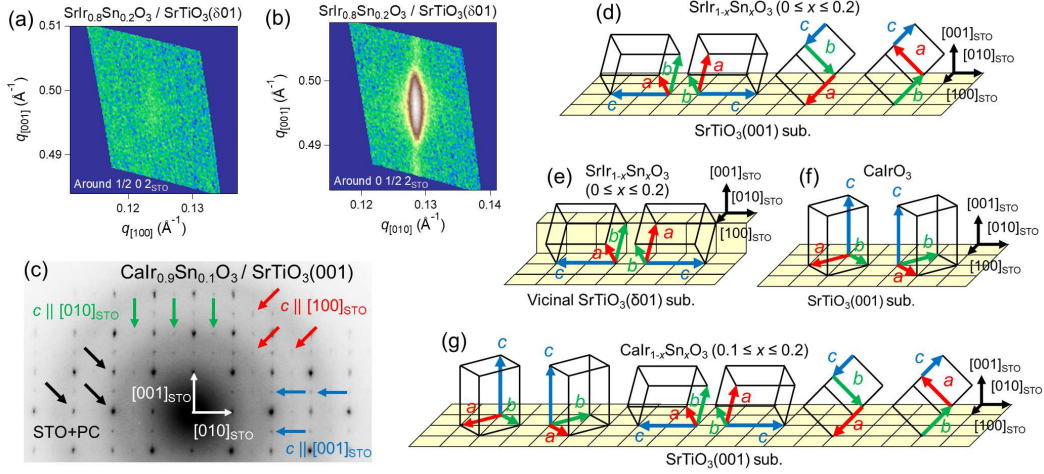


Fig. 2. The orientation of $\text{SrIr}_{1-x}\text{Sn}_x\text{O}_3$ and $\text{CaIr}_{1-x}\text{Sn}_x\text{O}_3$ films by XRD-RSM and transmission electron microscopy. XRD-RSM around $1/2\ 0\ 2_{\text{STO}}$ (a) and $0\ 1/2\ 2_{\text{STO}}$ (b) for $\text{SrIr}_{0.8}\text{Sn}_{0.2}\text{O}_3$ films grown on vicinal $\text{SrTiO}_3(\delta 01)$ substrates. The intensity of film peaks around $0\ 1/2\ 2_{\text{STO}}$ are significantly stronger than those around $1/2\ 0\ 2_{\text{STO}}$ (and $0\ 1\ 5/2_{\text{STO}}$, not shown), indicating the preferred orientation of c axis parallel to $[010]_{\text{STO}}$. The comparison of peak intensities of $1/2\ 0\ 2_{\text{STO}}$ and $0\ 1/2\ 2_{\text{STO}}$ peaks normalized with the substrate peaks indicates the ratio of domains with the preferred orientation as 95.4 % for $x = 0$ (data not shown), and 99.0 % for $x = 0.2$, respectively. (c) The electron diffraction pattern of $\text{CaIr}_{0.9}\text{Sn}_{0.1}\text{O}_3$, indicating the coexistence of domains with the doubled c axis perpendicular to the plane as observed in CaIrO_3 and those with the doubled c axis lying in the plane (green and red). Schematic pictures of crystalline orientations of $\text{SrIr}_{1-x}\text{Sn}_x\text{O}_3$ and $\text{CaIr}_{1-x}\text{Sn}_x\text{O}_3$ films with respect to $\text{SrTiO}_3(001)$ substrate. $\text{SrIr}_{1-x}\text{Sn}_x\text{O}_3$ on $\text{SrTiO}_3(001)$ (d) and on vicinal $\text{SrTiO}_3(\delta 01)$ (e). $\text{CaIr}_{1-x}\text{Sn}_x\text{O}_3$ with $x \sim 0$ (f) and $x \geq 0.1$ (g). The black boxes and the arrows labeled by a , b and c indicate the bulk unit cells of the film layers.

clear anisotropy of magnetization within the substrate plane was observed for $x = 0.2$ sample on the vicinal substrate as we describe below. Pronounced anisotropy in the magnetization was not observed in the resistivity $\rho(T)$.

The resistivity $\rho(T)$ measurements on the $\text{SrIr}_{1-x}\text{Sn}_x\text{O}_3$ films indicate the presence of a metal-insulator transition accompanied by a weak ferromagnetism as in the bulk¹⁷. The SrIrO_3 ($x = 0$) film shows only weakly temperature-dependent behavior of $\rho(T)$, where a gradual increase followed by the temperature-independent behavior is observed with decreasing temperature (Fig. 3a). This agrees well with previous reports on SrIrO_3 thin films^{15,23} and can be understood as a typical behavior of semimetals with extra conductivity at high temperature from thermally excited electrons and holes. With Sn doping (Fig. 3b), we do not observe an appreciable change of the $\rho(T)$ up to the critical concentration $x_c = 0.1$. Above $x_c = 0.1$, however, the resistivity shows a transition from the semimetal to a weak insulator at a transition temperature T_c where we observe a kink in $\rho(T)$ and a well-defined peak of the second derivative $d^2\rho(T)/dT^2$ (Fig. 3c). T_c increases rapidly with increasing x . The metal-insulator transition below T_c is accompanied by a weak ferromagnetism with the easy axis parallel to the pseudo-cubic c_{pc} axis (\parallel orthorhombic c), as seen in Fig. 3d. This behavior, the emergence of the magnetic insulator out of the Dirac node semimetal with Sn doping, can be summarized as a Sn content x - T phase diagram on top of contour map of the magnitude of $\rho(T)$ (Fig. 3e). The stabilization of the magnetic insulator phase at low temperatures above $x_c = 0.1$ highly likely originates from the increase of the effective electron correlation. We argue that this is because of the reduced hopping of $J_{\text{eff}} = 1/2$ electrons by the

introduction of Sn^{4+} without conduction electrons.

We find contrasting behavior in the Sn doping effect on $\rho(T)$ in $\text{CaIr}_{1-x}\text{Sn}_x\text{O}_3$ compared to $\text{SrIr}_{1-x}\text{Sn}_x\text{O}_3$. For CaIrO_3 ($x = 0$) films (Fig. 3a), the overall behavior of $\rho(T)$ is similar to that observed in SrIrO_3 . The magnitude of resistivity is, however, appreciably larger than that of SrIrO_3 . A weak increase of $\rho(T)$, reminiscent of a weak localization and not observed in SrIrO_3 , is seen below 20 K, which is suggestive of the presence of appreciable disorder effect. It was discussed in the recent transport study on single crystal CaIrO_3 that the Fermi level is much closer to the Dirac nodes and hence the electron and the hole densities are lower in CaIrO_3 than SrIrO_3 due to the enhanced correlation effect originating from the narrow band in CaIrO_3 ¹⁴. The effect of disorder should be enhanced in CaIrO_3 because of the reduced carrier density, which may account for the larger resistivity and the weakly localized behavior.

With Sn substitution, $\rho(T)$ gradually increases and shows a poorly insulating behavior with a power-law divergence (Figs. 4a, b). We do not see a well-defined semimetal-insulator transition as a function of T and x in contrast to the case for SrIrO_3 . We argue that the gradual transition from the Dirac node semimetal to a weak insulator is driven by the disorder and perhaps the inhomogeneity, and that the nature of semimetal-insulator transition is distinct from that of SrIrO_3 . It is natural that the effect of disorder associated with Sn-doping is much more profound in CaIrO_3 than in SrIrO_3 because of the lower carrier density and Fermi energy of CaIrO_3 . For $\text{CaIr}_{0.8}\text{Sn}_{0.2}\text{O}_3$, a very weak ferromagnetic moment appears to emerge below $T_{\text{mag}} \sim 100$ K with B perpendicular to the film plane, smaller in magnitude and lower in temperature

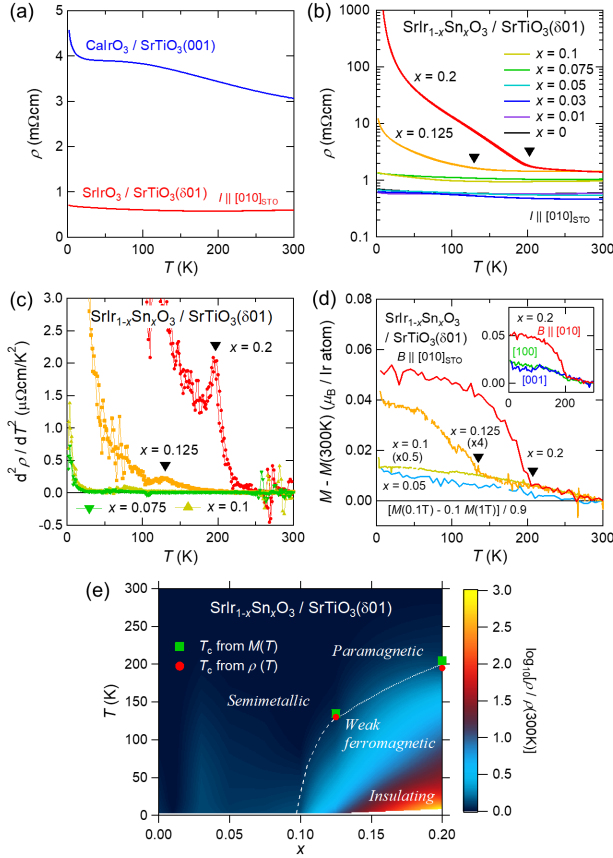


Fig. 3. (a) Temperature-dependent resistivity $\rho(T)$ of SrIrO_3 and CaIrO_3 . (b) $\rho(T)$ of $\text{SrIr}_{1-x}\text{Sn}_x\text{O}_3$ and (c) their second derivative. (d) Temperature-dependent magnetization $M(T)$ of $\text{SrIr}_{1-x}\text{Sn}_x\text{O}_3$ measured in the external field $B \parallel [010]_{\text{STO}}$. The background contributions including that from the contaminated oxygen was subtracted by taking the difference between 0.1 T and 1 T data as $M(T) = [M(T, B = 0.1 \text{ T}) - 0.1M(T, B = 1 \text{ T})]/0.9$. A weak ferromagnetic moment was not observed for the other magnetic field directions $B \parallel [100]$ and $[001]$ as shown in the inset. (e) The weak ferromagnetic transition temperature (the green squares) and the temperature where the resistivity has the anomaly (the red circles). The color plot shows the ratio of $\rho(T)$ and $\rho(T = 300 \text{ K})$ in logarithmic scale.

than $\text{SrIr}_{0.8}\text{Sn}_{0.2}\text{O}_3$ as shown in Fig. 4c. No clear anomaly can be identified in $\rho(T)$ at T_{mag} and $\rho(T)$ shows an insulating behavior above T_{mag} , implying that the magnetic ordering is not a trigger of the semimetal-insulator transition in $\text{CaIr}_{1-x}\text{Sn}_x\text{O}_3$ in contrast to that in $\text{SrIr}_{1-x}\text{Sn}_x\text{O}_3$. The emergence of magnetism in the disordered insulator may suggest a Mott insulator character and therefore a Mott-Anderson type metal-insulator transition in $\text{CaIr}_{1-x}\text{Sn}_x\text{O}_3$.

In summary, we have successfully grown thin films of Dirac semimetals $\text{SrIr}_{1-x}\text{Sn}_x\text{O}_3$ and $\text{CaIr}_{1-x}\text{Sn}_x\text{O}_3$ epitaxially on $\text{SrTiO}_3(001)$, with their orthorhombic c axis parallel and perpendicular to the substrate plane respectively. In the case of $\text{SrIr}_{1-x}\text{Sn}_x\text{O}_3$, the c axis can be aligned within the substrate plane using a vicinal substrate. While a well-defined Dirac node semimetal to a magnetic insulator transi-

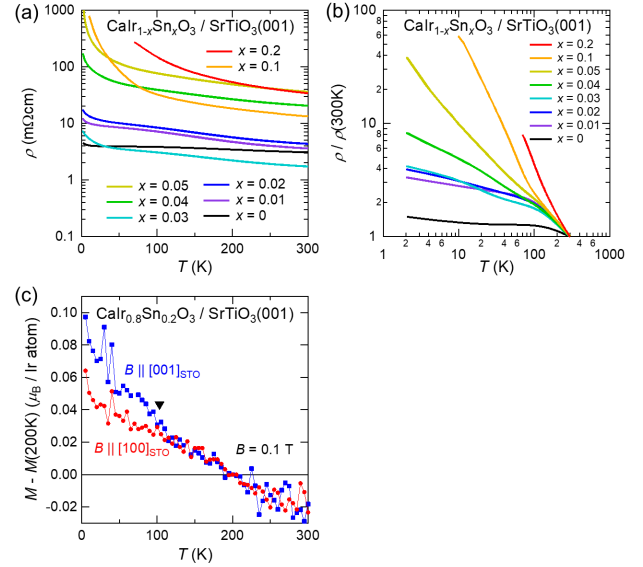


Fig. 4. (a) Temperature-dependent resistivity $\rho(T)$ of $\text{CaIr}_{1-x}\text{Sn}_x\text{O}_3$ thin films and (b) the ratio of $\rho(T)$ in (a) and $\rho(T = 300 \text{ K})$, indicating power-law temperature dependence. (c) Temperature-dependent magnetization $M(T)$ of $\text{CaIr}_{0.8}\text{Sn}_{0.2}\text{O}_3$ thin film, plotted as the difference from $M(T = 200 \text{ K})$. An additional contribution to the uncompensated offset can be seen below $T \sim 100 \text{ K}$ for $B \parallel [001]_{\text{STO}}$.

tion with Sn doping is observed at a critical Sn concentration $x_c \sim 0.1$ in $\text{SrIr}_{1-x}\text{Sn}_x\text{O}_3$, we observe in $\text{CaIr}_{1-x}\text{Sn}_x\text{O}_3$ that the Dirac node semimetal changes only gradually to a poor insulator without any well-defined semimetal-insulator transition. We argue that the contrast between $\text{SrIr}_{1-x}\text{Sn}_x\text{O}_3$ and $\text{CaIr}_{1-x}\text{Sn}_x\text{O}_3$ is a consequence of the interplay between the enhanced effective electron correlation and the disorder effect by Sn doping. While the correlation effect dominates in the case of $\text{SrIr}_{1-x}\text{Sn}_x\text{O}_3$, the disorder effect and the carrier localization dominate in the $\text{CaIr}_{1-x}\text{Sn}_x\text{O}_3$ due to the proximity of the Fermi level to the Dirac nodes and the resultant low carrier concentration. These results clearly indicate that Sn-doped iridium perovskite oxides are an interesting playground to study the effect of electron correlations and disorders in a topological semimetal.

ACKNOWLEDGMENTS

This work was supported by JSPS KAKENHI Grant Number JP24224010, JP17H01140, JP15H06092, JP17K14335 and JP18J21922.

¹W. Witczak-Krempa, G. Chen, Y. B. Kim, and L. Balents, Annual Review of Condensed Matter Physics **5**, 57–82 (2014).

²V. M. Katukuri, H. Stoll, J. van den Brink, and L. Hozoi, Phys. Rev. B **85**, 220402(R) (2012).

³S. J. Moon, H. Jin, K. Kim, W. S. Choi, Y. S. Lee, J. Yu, G. Cao, A. Sumi, H. Funakubo, C. Bernhard, and T. W. Noh, Phys. Rev. Lett. **101**, 226402 (2008).

⁴B. J. Kim, H. Jin, S. J. Moon, J.-Y. Kim, B.-G. Park, C. S. Leem, J. Yu, T. W. Noh, C. Kim, S.-J. Oh, J.-H. Park, V. Durairaj, G. Cao, and E. Rotenberg, Phys. Rev. Lett. **101**, 076402 (2008).

- ⁵B. J. Kim, H. Ohsumi, T. Komesu, S. Sakai, T. Morita, H. Takagi, and T. Arima, *Science* **323**, 1329–1332 (2009).
- ⁶H. Takagi, T. Takayama, G. Jackeli, G. Khaliullin, and S. E. Nagler, *Nat. Rev. Phys.* **1**, 264–280 (2019).
- ⁷J. M. Longo, J. A. Kafalas, and R. J. Arnett, *Journal of Solid State Chemistry* **3**, 174–179 (1971).
- ⁸C. L. McDaniel and S. J. Schneider, *Journal of Solid State Chemistry* **4**, 275–280 (1972).
- ⁹J. M. Carter, V. V. Shankar, M. A. Zeb, and H.-Y. Kee, *Phys. Rev. B* **85**, 115105 (2012).
- ¹⁰Y. Chen, H.-S. Kim, and H.-Y. Kee, *Phys. Rev. B* **93**, 155140 (2016).
- ¹¹Y. F. Nie, P. D. C. King, C. H. Kim, M. Uchida, H. I. Wei, B. D. Faeth, J. P. Ruff, J. P. C. Ruff, L. Xie, X. Pan, C. J. Fennie, D. G. Schlom, and K. M. Shen, *Phys. Rev. Lett.* **114**, 016401 (2015).
- ¹²Z. T. Liu, M. Y. Li, Q. F. Li, J. S. Liu, W. Li, H. F. Yang, Q. Yao, C. C. Fan, X. G. Wan, Z. Wang, and D. W. Shen, *Sci. Rep.* **6**, 30309 (2016).
- ¹³J. Fujioka, T. Okawa, A. Yamamoto, and Y. Tokura, *Phys. Rev. B* **95**, 121102(R) (2017).
- ¹⁴J. Fujioka, R. Yamada, M. Kawamura, S. Sakai, M. Hirayama, R. Arita, T. Okawa, D. Hashizume, M. Hoshino, and Y. Tokura, *Nat. Comm.* **10**, 362 (2019).
- ¹⁵J. Matsuno, K. Ihara, S. Yamamura, H. Wadati, K. Ishii, V. V. Shankar, H.-Y. Kee, and H. Takagi, *Phys. Rev. Lett.* **114**, 247209 (2015).
- ¹⁶R. D. Shannon, *Acta Cryst. A* **32**, 751 (1976).
- ¹⁷Q. Cui, J.-G. Cheng, W. Fan, A. E. Taylor, S. Calder, M. A. McGuire, J.-Q. Yan, D. Meyers, X. Li, Y. Q. Cai, Y. Y. Jiao, Y. Choi, D. Haskel, H. Gotou, Y. Uwatoko, J. Chankhalian, A. D. Christianson, S. Yunoki, J. B. Goodenough, and J.-S. Zhou, *Phys. Rev. Lett.* **117**, 176603 (2016).
- ¹⁸B. L. Chamberland and A. R. Philpotts, *Journal of Alloys and Compounds* **182**, 355–364 (1992).
- ¹⁹Strictly speaking, in both SrIrO₃ and CaIrO₃, cells of film layers on SrTiO₃(001) slightly deform from orthorhombic to monoclinic due to epitaxial strain.
- ²⁰D. Hirai, J. Matsuno, D. Nishio-Hamane, and H. Takagi, *Appl. Phys. Lett.* **107**, 012104 (2015).
- ²¹L. Zhang, H.-Y. Wu, J. Zhou, F.-X. Wu, Y. B. Chen, S.-H. Yao, S. Zhang, and Y. Chen, *Applied Surface Science* **280**, 282–286 (2013).
- ²²A. K. Jaiswal, R. Schneider, R. Singh, and D. Fuchs, (2019), arXiv:1907.07520.
- ²³L. Zhang, B. Pang, Y. B. Chen, and Y. Chen, *Critical Reviews in Solid State and Materials Sciences* **43:5**, 367–391 (2018).